

A New Force/Torque Sensor for Robotic Applications Based on Optoelectronic Components[†]

C. Melchiorri, L. Moriello, G. Palli and U. Scarcia

Abstract—In this paper, a novel force/torque sensor is presented. The sensor is based on optoelectronic components and therefore its design is relatively simple and reliable. The sensor design make it suitable for the integration in different robotic systems, such as e.g. the fingers of robotic hands. The basic principle and the design of the sensor are described in this paper, along with a specific prototype implemented for underwater applications. Experimental data are presented and discussed to illustrate the main features of the proposed sensor, and its use as an intrinsic tactile sensor is evaluated.

Index Terms—Force/Torque Sensors, Optoelectronic Sensors, Dexterous Manipulation, Intrinsic Tactile Sensors.

I. INTRODUCTION

The sense of touch is essential to properly manipulate objects. The importance of having a proper sensing of the contact forces exerted during manipulation tasks is proved by the huge amount of work in tactile sensing literature. Despite this, the design of reliable and accurate tactile sensors has proven to be very hard, and relatively few commercial devices are currently available, mainly due to high manufacturing complexity and cost. Many different designs have been proposed, and almost every kind of physical transduction principle has been exploited to obtain a tactile sensor. A recent and complete review on tactile sensors's technologies and features is reported e.g. in [1]. With particular reference to optical-based devices, many technologies have been proposed. A very common technology is based on Fibre Bragg Gratings (FBG), exploiting the relationship between the variations of the FBG wavelength and the external force applied to the FBG [2]. Other well known sensors are based on CCD or CMOS camera to capture the deformation of a surface caused by the external force [3]. Both technologies are expensive, difficult to integrate into complex robotic systems (e.g. anthropomorphic hands, robotic arms) and involve high computational costs. Many other clever solutions are based on discrete optoelectronic components. In these cases, the sensor exploits the scattering or the reflection of a light beam. Examples of scattering-based sensors are reported in [4] and [5], in which the light beam of an light emitting diode (LED)

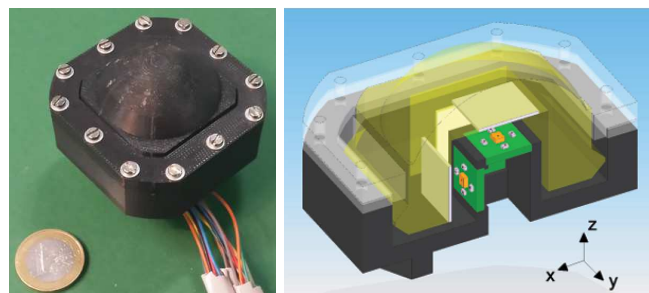


Fig. 1. The optoelectronic sensor and its CAD representation.

is scattered by a silicon dome and a urethane foam cavity respectively. In both cases the working principle is the same: the compression of the dome or the cavity due to applying an external force, causes a scattered energy density variation that is detected by several photodetector (PD). Particularly noticeable is the research in the field of optical force/torque sensors carried out by Hirose and Yoneda [6]. They adopted a 2-axes photosensor for the implementation of an optical 6-axes force/torque sensor. Another interesting example of optical tactile sensor can be found in [7], in which a matrix of LED/PD couples is covered by a deformable elastic layer. In that case, the working principle is the union of cavity scattering principle mentioned before, and of a taxel-based reconstruction typical of CMOS sensors. In [8] instead, it is described an example of a tactile/force sensor which exploits the reflection of a light cone from a LED on a silicon rubber dome. In this case, the force reconstruction is related to the spatial distribution of the radiation intensity after the reflection of the light on the deformable dome above the optical components.

The 6-axes force/torque (F/T) sensor presented in this paper exploit the optical reflection concept mentioned above, in order to obtain an easily scalable and low cost intrinsic tactile sensor. The proposed sensor is characterized by a natural robustness with respect to electromagnetic noise due to the adoption of optical components, and requires an extremely simple conditioning electronics. Moreover, the exploitation of the light reflection simplify the cabling, making it easy to integrate the sensor into complex robotic structures such as robotic hands. This paper is structured as follows. In Sec. II the principle of the sensor is described and the design of a

C. Melchiorri, L. Moriello, G. Palli and U. Scarcia are with DEI - Department of Electrical, Electronic and Information Engineering - University of Bologna, Italy (email: claudio.melchiorri@unibo.it).

This work is supported by the Italian National Project MARIS "Marine Autonomous Robotics for InterventionS".

[†]Patent pending.

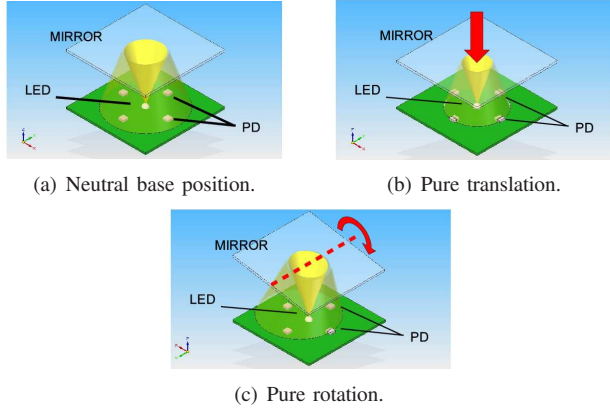


Fig. 2. Reflection of an ideal cone of light

prototype reported. Note that the developed sensor is going to be installed on a three-fingered gripper for underwater tasks, and therefore some design choices have been conditioned by this particular application. In Sec. III experimental results are described and discussed, while Sec. IV concludes with final remarks and plans for future activity.

II. SENSOR CONCEPT AND DESIGN

The working principle of the proposed sensor is based on the modulation of the current flowing through a PD caused by the power variation of the received light generated by an infrared source such as an LED. In our design, the light power variation is due to the variation of both the angle of view and the length of the optical path between the optoelectronic components [9]. Assuming a single LED and a certain number of PDs arranged on the same plane (mounted on the same electronic board), and a reflective layer (a mirror) located above the electronic board able to move with respect to the board plane. As seen for tactile sensors, e.g. [7], the principle is to reconstruct the applied force by measuring the motion/deformation of the elastic layer on which the reflection or scattering of light occurs. In this case, the reflective layer is not deformable, but it can move if an external force is applied. Therefore, the idea is to obtain position and orientation of the mirror (and then the applied force and torque) from the light intensity measured by photodiodes, i.e. from the spatial distribution of reflected light cone.

A. Sensor Model and Validation

As a first design step, a numerical model of the proposed sensor has been developed and tested in simulation. The model is based on the simplifying assumptions of geometrical optics: light rays propagation always follow a rectilinear path as far as they travel in a homogeneous medium. Figure 3 shows a LED and a PD mounted on the surface of a Printed Circuit Board (PCB). In this configuration, the light path depends on the distance d and orientation φ of the mirror, on which reflection is assumed to be specular as described

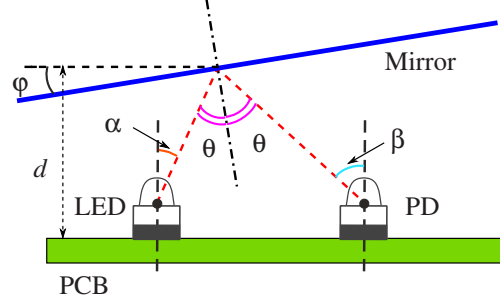


Fig. 3. Interaction between the optoelectronic components.

by the reflection law. Thus, the model compute the path defining first an hypothetical triangle which lies on the perpendicular plane of the mirror passing through the LED and the photodiode, and having the reflection point, the LED, and the PD positions as corners. Moreover the angle at the reflection point corner must be 2θ in agreement with the reflection law. This geometrical approach allows to obtain the radiation and reflection angles and the length l of the optical path as the sum of the distances from the LED to the reflection point and from the PD to the reflection point.

The model also takes into account the reflection coefficient of the mirror. In Fig. 3, α represents the angle between the LED mechanical axis and the segment that denotes the light path, while β represents the angle between the PD mechanical axis and the light path. The viewing angle between the two components depends by the reflection angle θ and by the mirror orientation φ . In this state a certain amount of light emitted by the LED reaches the PD and it is proportionally converted into an electrical current, $I_p(\alpha, \beta)$. Recalling the theory on LED radiation patterns [9], it is possible to model the interaction of the optoelectronic components. In particular, if the length of the light path is large enough to render the far-field approximation valid, the LED and the PD could be regarded as a point source and a point receiver, respectively. In this case the photocurrent $I_p(\alpha, \beta)$ will be proportional to the product between the radiant intensity pattern of the LED, evaluated in α (denoted as $\mathcal{L}(\alpha)$) and the responsivity pattern of the PD, evaluated in β (denoted as $\mathcal{R}(\beta)$), and inversely proportional to the square of the light path length l

$$I_p(\alpha, \beta) = K \frac{\mathcal{L}(\alpha) \mathcal{R}(\beta)}{l^2} \quad (1)$$

where K is a proper constant.

When the mirror orientation φ and distance d from the PCB experience a variation with respect to their initial values, the light path changes and a different amount of light power will be sensed by the PD and a current variation occurs. This happens because both the radiation pattern of the LED and the responsivity pattern of the PD vary with the angles. Moreover, the light path length changes with the mirror orientation and distance. The combination of these effects leads to the observed variations of the photocurrent. The

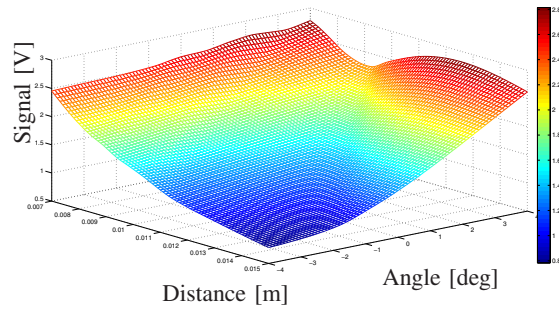


Fig. 4. Output of the model as a function of angle and distance of the reflecting plane.

radiant intensity pattern of the LED $\mathcal{L}(\cdot)$ and the responsivity pattern of the PD $\mathcal{R}(\cdot)$ are available from the data-sheets of the components.

The model has been developed taking as basic components an infrared LED with a narrow viewing angle and with a typical peak wavelength of 850 nm (Vishay VSMY2850G), and a silicon NPN phototransistor (Osram SFH3010) as PD with a maximum peak sensitivity at 860 nm wavelength. An LED with a narrow viewing angle has been chosen to avoid that the PD is illuminated by direct light from the LED (without being reflected first). Considering a LED/PD couple arranged on a printed circuit board at a distance of 6 mm, Fig. 4 reports the PD output voltage for different values of the distance and orientation of the mirror. This figure shows a quite complex behaviour of the received light power modulated by the mirror motion. However, two main aspects are visible:

- The PD signal rapidly decreases while the distance increases, as a consequence of the increasing optical path length, related to the light intensity by the inverse-square law;
- The angular modulation is a combination of the path length variation and the angular displacement effects. The choice of a narrow viewing angle LED is crucial to boost this effect and allows to obtain good sensitivity also on very small angular displacements (few degrees).

In order to validate the model, a specific laboratory setup has been developed to move the reflecting mirror (translational and rotational motions) in a very precise and controlled way by means of two linear motors, and the output voltage of the PD has been measured and compared with the theoretical model, see Fig. 5. The maximum error between the model and the real data is about 10%, but in any case these results are quite satisfactory since they allow to verify in advance the characteristics of the sensor, based on a set of parameters (optoelectronic component selection and arrangement of both the components and the mirror). Moreover, although the obtained characteristic is nonlinear, it is interesting to note that in a region surrounding the centre of the plot (angle = 0°, distance \approx 10 mm) the outputs of both the model

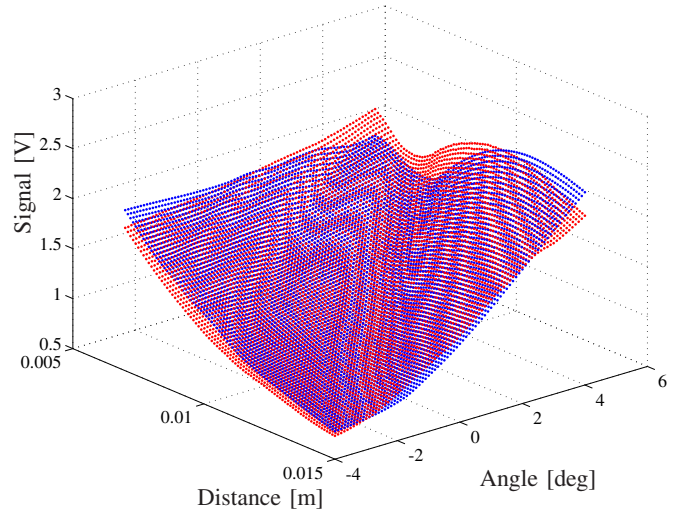


Fig. 5. Validation of the model (blue) compared with real data (red).

and the experimental device present a very limited difference and an almost linear behaviour. This allows to calibrate the sensor in a quite simple manner. Aiming at measuring the distance and the orientation of the mirror with respect to two orthogonal axis in the LED/PD plane, another experimental device composed by two pairs of PDs symmetrically arranged with respect to the LED has been designed. In this device, the LED/PD arrangement reproduces the one shown in Fig. 2. The results reported in Fig. 6 shown that this configuration allows to measure the distance and the rotation of the mirror, at least for limited displacements (± 1 deg).

B. Sensor Prototype

The solution with a LED and four PDs arranged around it is the basic element of the proposed F/T sensor. In order to reduce the overall dimensions, a smaller LED (OSRAM SFH4451) has been chosen and the PD have been arranged on a circle of radius 3 mm. This allows to obtain an electronic board of 1 cm². Furthermore, to be able to measure forces and torques along the three axes, 3 of these basic elements have been placed on three faces of a cube.

A prototype of the sensor is shown in Fig. 1 and Fig. 7. The three boards with the opto-components are fixed on the cubic structure in the core of the sensor. A specific mask with a hollow has been designed in order to avoid cross-disturbances (light reflections) between the three boards. The relative motion of the mirrors and the boards is achieved by o-ring seals, that deform in an elastic fashion when an external force is applied. Note that by changing these elastic elements (and in case the sensor design as well), it is possible to have different working ranges (in the force domain) for the sensor. The conditioning electronics is extremely simple, as usual for optical components, and consists only in a gain resistor. This aspect is quite important because it allows a simple integration of the sensor in mechanically complex structure.

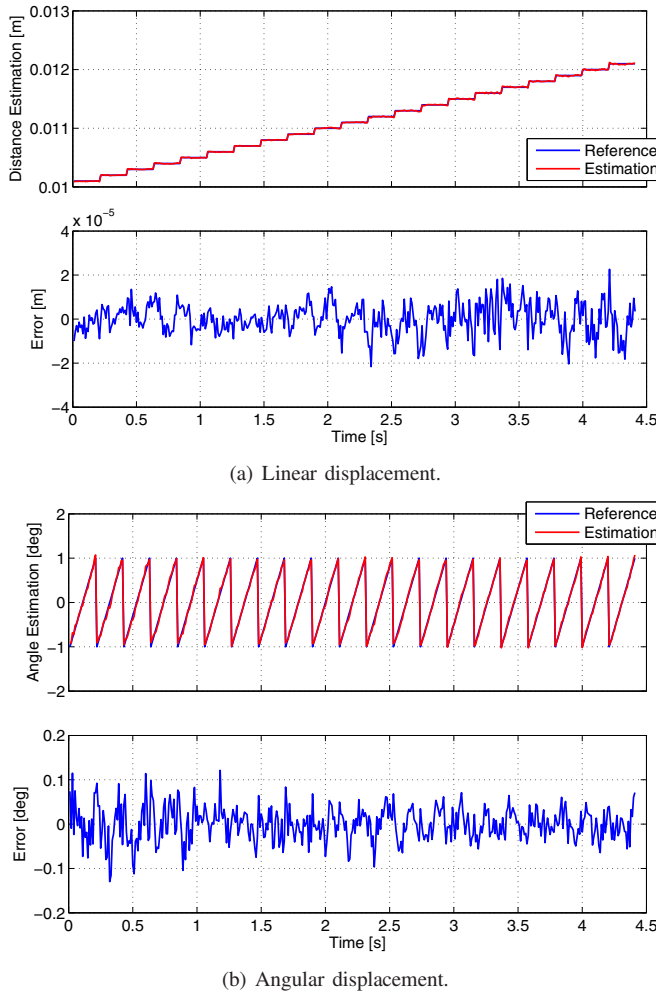


Fig. 6. Reconstruction of linear and angular displacement using a LED and two PDs.

The external surface of the sensor is, in this specific prototype, a portion of a spherical surface with radius $R = 21.5$ mm. This particular design has been developed since the sensor is going to be placed on the fingertips of a underwater three-fingered robot gripper, [10], and both the dimension and some of the design choices (e.g. the o-rings for water insulation) derive from this specific application. In particular, the overall dimension of the sensor could be drastically reduced for other types of applications.

III. CALIBRATION AND CHARACTERIZATION

For the calibration and the experimental characterization of the sensor, a laboratory setup has been developed, see Fig. 8, consisting in a linear motor LinMot-37x160 equipped with a precision load cell, and an ATI Gamma SI-130-10 F/T sensor. The linear motor is used to apply the desired force to the optoelectronic force sensor along the motor axis, and is also equipped with an integrated encoder to measure the motor position. The linear motor is driven by a low-level control system that allows to apply the desired force

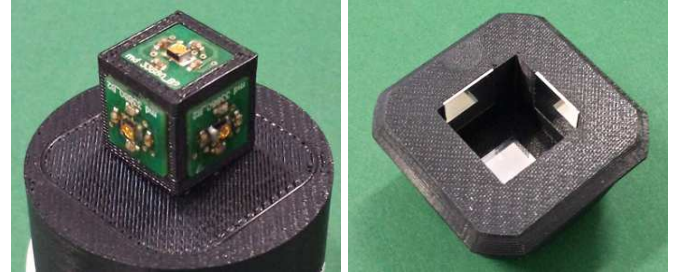


Fig. 7. Internal view of the sensor: the cube with the three electronic boards and the cover with the mirrors.

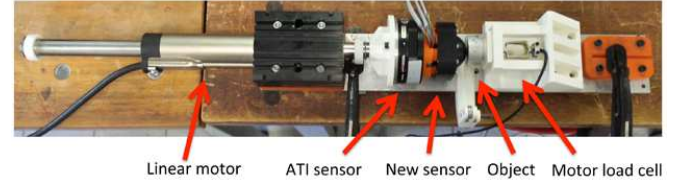


Fig. 8. Laboratory setup for calibration and experimental validation.

profile compensating for the friction acting on the motor slider [11]. The controller and the data acquisition system are implemented by a PC-104 with Intel ATOM processor running the RTAI-Linux realtime OS. The software design is performed using MatLab, Simulink and the Realtime Workshop by a Linux workstation, that is also used as user interface for the control and acquisition system.

A. Sensor Calibration

The calibration procedure has been performed by mounting the prototype on the reference ATI sensor and acquiring data from both sensors while applying a set of forces and torques. In fact, as mentioned in Sec. II-A, being the sensor working in the linear area and considering an elastic deformation of the o-rings, it can be assumed that a linear function exists between the applied force/torque vector $w = [f^T, m^T]^T$ and the output v of the PDs, given by $w = Cv$, where $C \in \mathbb{R}^{6 \times 12}$ is the calibration matrix. For this reason, the calibration is quite simple and consists in applying a set of force/torque vectors $W = [w_1, w_2, \dots, w_n] \in \mathbb{R}^{6 \times n}$, measured by the reference sensor, collecting the relative set of output voltages $V = [v_1, v_2, \dots, v_n] \in \mathbb{R}^{12 \times n}$, and finally computing the calibration matrix C as

$$C = W V^+$$

being V^+ the pseudo-inverse of V . Once the calibration matrix is obtained, the vector w of forces/torques applied to the sensor is simply computed from the PD values v as $w = Cv$. Notice that the forces are expressed in a reference frame with origin in the centre of the sensor and axes direct as shown in Fig. 1. Because of the specific mechanical design¹,

¹As already mentioned, the mechanical and elastic part of the sensor can be tailored for specific applications, and therefore different performances can be achieved if desired.

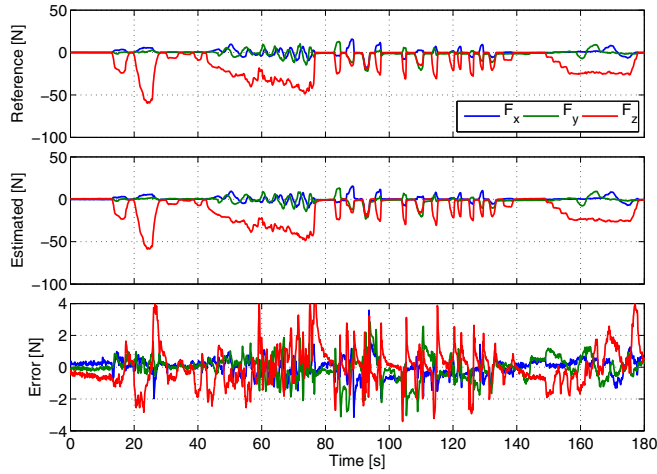


Fig. 9. Force reconstruction after calibration.

the operating range of the sensor is $[0 \div 100]$ N for forces along the z direction, and $[-50 \div 50]$ N in the $x-y$ plane, while torques are limited to $[-5 \div 5]$ Nm along the three axes. Fig. 9 shows a test in which forces are measured by the reference sensor and by the new sensor after calibration, and the difference among them. From the plots, and in particular from the plot of the difference, it can be noticed that there are some “peaks” when the applied force has a sudden change. These peaks are due to the different elastic properties of the two sensors (the o-rings have a more evident visco-elastic behaviour).

B. Sensor Performance

In order to fully characterize from a static and dynamic point of view the sensor, other experiments have been performed. In particular, the sensor has been installed on the setup of Fig. 8 in order to apply precise axial forces (z direction).

For example, Fig. 10 shows a test in which a sinusoidal force with constant frequency (0.1 Hz) and increasing amplitude is applied by the motor along the z axis. It is possible to see an increasing error when the force gradient becomes larger and larger. As a matter of fact, because of the visco-elastic properties of the rubber used to seal the optical sensor, this is ‘slower’ than the reference sensor in recovering the unloaded position. This effect is more evident in Fig. 11 where a 20 N sinusoidal force is applied at increasing frequencies, from 0.01 to 3 Hz. The error increases with the frequency of the input signal.

However, it has to be pointed out that this effect is not due to some intrinsic limitations of the basic principle of the sensor, but rather to the particular mechanical design employing rubber sealing.

C. Evaluation of the Friction Coefficient

Another experiment is reported in and Fig. 12, where a constant force along the z direction is applied to an object. On

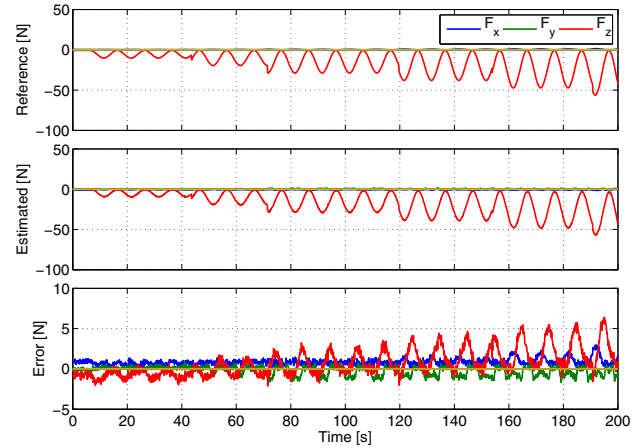


Fig. 10. Application of a sinusoidal force signal with increasing amplitude at 0.1 Hz.

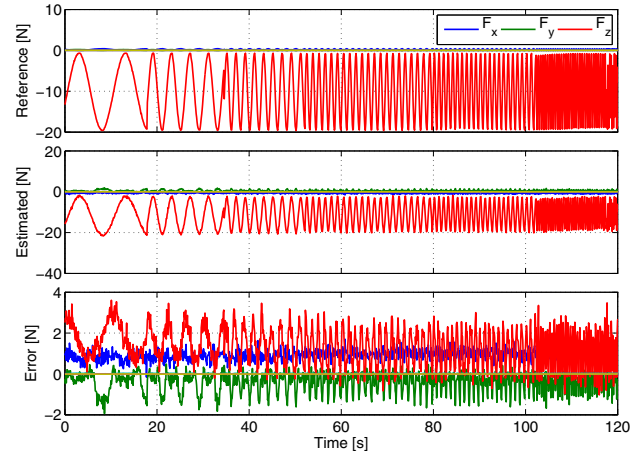


Fig. 11. Application of a sinusoidal force signal (20 N) at increasing frequencies.

the object, an external increasing force is applied as well (by means of some weights) and therefore the sensor measures both the normal (z axis) and tangential ($x-y$ plane) forces (f_n, f_t). In the experiment, the object was covered by a silicon rubber to increase friction (the surface of the sensor, built with 3D printing technology, has a very low friction coefficient), and the applied tangential forces were $f_t = 3, 8, 13, 18$ N, while the normal force was $f_n = 30$ N. Notice that with the load of $f_t = 13$ N, the object starts to slide. The decrease of the normal force f_n when the tangential component is $f_t = 13$ N is due to the non negligible deformation of the silicon rubber covering the object. This type of experiment allows also to estimate the friction coefficient $\mu = f_t / f_n$ and to implement some control strategies in order to avoid slippage of the object.

D. Characterization as Intrinsic Tactile Sensor

Among the many usages for force/tactile sensors, in the literature it has been described by several authors how to use them in robotic applications for the computation, besides of applied force/torque vectors, also of the contact point between e.g. the fingers of a robot hand and the grasped

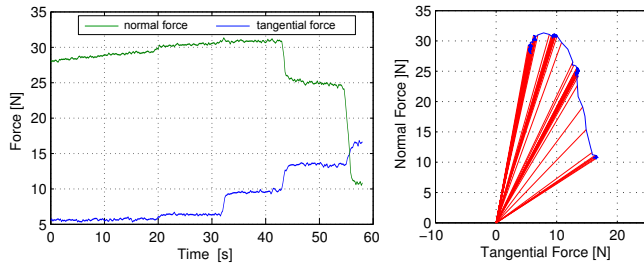


Fig. 12. Measurement of the normal and tangential forces.

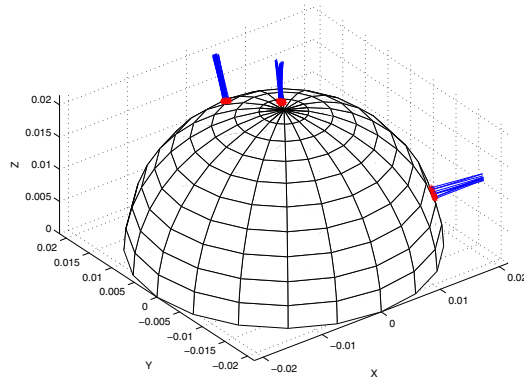


Fig. 13. Measurement of the applied forces and of the contact point.

object, see [12], [13], [14], [15]. Considering a ‘hard finger’ contact (i.e. locally only forces and not torques can be applied at the contact), the same principle has been tested with the new sensor. As described e.g. in [13], in case of a sensor with spherical surface (with radius R) the position p_c of the contact point can be obtained from the force f and torque m measured by the F/T sensor from

$$\begin{aligned}\lambda &= -\frac{1}{\|f\|} \sqrt{R^2 - \frac{\|f \times m\|^2}{\|f\|^4}} \\ r_0 &= \frac{f \times m}{\|f\|^2} \\ p_c &= r_0 + \lambda f\end{aligned}$$

Since two solution are obtained from these equations (solution of the intersection of a line with a sphere), the point for which the force is entering the surface must be selected. Typical results are reported in Fig. 13, where the applied forces are shown as lines and the contact points are measured on the surface of the sensor. In this test, three forces are applied at three different points, whose $[x, y, z]$ coordinates have been computed as $[1.2, 2.1, 21.1]$ mm, $[-1.4, 10.7, 18.1]$ mm and $[17.6, -7.8, 5.4]$ mm, corresponding to radii of 21.2, 21.1 and 20.0 mm respectively (the radius of the spherical surface is 21.5 mm).

IV. CONCLUSIONS

In this paper, a novel force/torque sensor for robotic application has been presented and some preliminary results obtained with a first prototype reported and discussed. The

sensor is based on optoelectronic components and therefore is a low-cost, simple and reliable device. Moreover, it is easily integrable in relatively complex devices from both the mechanical and electronic point of view. The sensor has been designed to be placed in the fingertips of robot grippers or hands, and the particular prototype discussed in this paper has been developed for a three-fingered gripper for underwater applications. The experimental results confirm the satisfactory performances of the sensor, that can be used not only for measuring the external force/torque vector applied to it, but also as a ‘intrinsic tactile’ sensor able to determine the position of the contact point. Activity is in progress to characterise different elastic materials (to be used to obtain sensors with different working ranges), to identify different mechanical configurations, and to develop more compact sensors for other type of applications.

REFERENCES

- [1] R. Dahiya, G. Metta, M. Valle, and G. Sandini, “Tactile sensing from humans to humanoid,” *IEEE Transactions on Robotics*, vol. 26, no. 1, pp. 1–20, 2010.
- [2] J. Heo, J. Chung, and J. Lee, “Tactile sensor arrays using fiber bragg grating sensors,” *Sensors and Actuators A: Physical*, vol. 126, no. 2, pp. 312–327, 2006.
- [3] K. Kamiyama, K. Vlack, T. Mizota, H. Kajimoto, N. Kawakami, and S. Tachi, “Vision-based sensor for real-time measuring of surface traction fields,” *Computer Graphics and Applications, IEEE*, vol. 25, no. 1, pp. 68–75, 2005.
- [4] R. C. E. Torres-Jara, I. Vasilescu, “A soft touch: compliant tactile sensors for sensitive manipulation,” in *CSAIL Technical Report MIT-CSAIL-TR-2006-014*, 2006.
- [5] R. R. G. Hellard, “A robust, sensitive and economical tactile sensor for a robotic manipulator,” in *Proc. of Australasian Conference on Robotics and Automation*, 2002, pp. 100–104.
- [6] S. Hirose and K. Yoneda, “Development of optical 6-axial force sensor and its signal calibration considering non linear calibration,” in *Proc. IEEE Int. Conf. on Robotics and Automation*, vol. 1, Tsukuba, Japan, 1990, pp. 46–53.
- [7] G. De Maria, C. Natale, and S. Pirozzi, “Tactile sensor for human-like manipulation,” in *Proc. IEEE RAS EMBS Int. Conf. on Biomedical Robotics and Biomechanics*, 2012, pp. 1686–1691.
- [8] A. Tar and G. Cserey, “Development of a low cost 3d optical compliant tactile force sensor,” in *Advanced Intelligent Mechatronics (AIM), 2011 IEEE/ASME International Conference on*, 2011, pp. 236–240.
- [9] S. Kasap, *Optoelectronics and Photonics: Principles and Practices*. Englewood Cliffs, NJ: Prentice Hall, 2001.
- [10] J. Bemfica, C. Melchiorri, L. Moriello, G. Palli, U. Scarcia, and G. Vassura, “Mechatronic design of a three-fingered gripper for underwater applications,” in *6th IFAC Symposium on Mechatronic Systems, Hangzhou, China*, 2013, pp. 307–312.
- [11] G. Palli and C. Melchiorri, “Velocity and disturbance observer for non-model based load and friction compensation,” in *Proc. Int. Workshop on Advanced Motion Control*, Trento, Italy, 2008, pp. 194–199.
- [12] J. Salisbury, “Interpretation of contact geometries from force measurements,” in *Robotics and Automation. Proceedings. 1984 IEEE International Conference on*, 1984, pp. 240–247.
- [13] A. Bicchi, J. Salisbury, and D. Brock, “Contact sensing from force measurements,” *International Journal of Robotics Research*, vol. 12, pp. 249–262, 1990.
- [14] A. Cicchetti, A. Eusebi, C. Melchiorri, and G. Vassura, “An intrinsic tactile force sensor for robotic manipulation,” in *Proc. 7th. Int. Conf. on Advanced Robotics, ICAR’95, Sant Feliu de Guixols, Spain*, 1995, pp. 889–894.
- [15] C. Melchiorri, “Tactile sensing for robotic manipulation,” in *Articulated and Mobile Robotics for Services and Technologies (RAMSETE)*. Springer, 2001, pp. 75–102.